Application and Extension of the Particle X-ray Coincidence Technique to Astrophysical Reaction Rates

L. J. Sun[a], J. Dopfer[b,a], A. Adams[b,a], C. Wrede[b,a,*], A. Banerjee[c], B. A. Brown[b,a], R. Mahajan[a], T. Rauscher[d,e], C. Sumithrarachchi[a], D. Weisshaar[a], T. Wheeler[b,a]

[a]*Facility for Rare Isotope Beams, Michigan State University, East Lansing, Michigan 48824, United States*
[b]*Department of Physics and Astronomy, Michigan State University, East Lansing, Michigan 48824, United States*
[c]*Saha Institute of Nuclear Physics, 1/AF, Bidhan Nagar, Kolkata 700064, India*
[d]*Department of Physics, University of Basel, 4056 Basel, Switzerland*
[e]*Centre for Astrophysics Research, University of Hertfordshire, Hatfield AL10 9AB, United Kingdom*

Abstract

Lifetimes of excited nuclear states are crucial in many aspects of nuclear physics, from nuclear structure to astrophysics. It has been demonstrated that the particle-X-ray coincidence technique (PXCT) developed based on an atomic clock technique can provide one of the best ways of probing the lifetimes of excited nuclear states in the time range of 10^{-17} – 10^{-15} s. We have developed a detection system at the Facilities for Rare Isotope Beams to extend this technique to measure the lifetimes of discrete resonances required for thermonuclear reaction rate calculations. The performance of the PXCT detectors has been thoroughly tested using radioactive sources. With an expected ^{60}Ga beam rate of 1.2×10^5 per second from the full-power FRIB, this system opens a path to significantly improved constraints on the strength of the NiCu cycle on the rapid proton capture process by measuring ^{60}Ga decay.

1. Introduction

In the 1970s, the Particle X-ray Coincidence Technique (PXCT) was initially demonstrated and applied to measure the average lifetimes of proton-unbound states in ^{69}As populated by the electron capture (EC) of ^{69}Se [1]. The principle of the method is illustrated in Fig. 1. In the process of an EC-delayed proton emission, a proton-rich precursor with an atomic number of Z decays by K-EC to the proton emitter $(Z-1)$. Due to the EC, a proton unbound nuclear state and an atomic shell vacancy are created simultaneously. An atomic electron in a higher-lying shell fills the vacancy with typical lifetimes of $\tau_{K\text{shell}} = 0.01$ to 1.0 fs and emits the characteristic X ray. Meanwhile, the proton-unbound state with a comparable lifetime $\tau_{p-\text{emit}}$ emits a proton to a state of the daughter $(Z-2)$. If the proton is emitted before the X-ray emission, then the characteristic X-ray energy will correspond to the atomic number of the daughter $(Z-2)$. If the proton is emitted after the X-ray emission, then the X-ray energy will be characteristic of the atomic number of the proton emitter $(Z-1)$. By measuring the spectrum of X rays in coincidence with protons and counting the relative intensities of the $Z-1$ and $Z-2$ X-ray peaks $I_{KX(Z-1)}/I_{KX(Z-2)}$, the lifetimes of proton-emitting states can be related to the lifetimes of the emitter K-shell vacancies by the relation

$$\frac{\tau_{p-\text{emit}}}{\tau_{K\text{shell}}} = \frac{\Gamma_{K\text{shell}}}{\Gamma_{p-\text{emit}}} = \frac{I_{KX(Z-1)}}{I_{KX(Z-2)}}, \quad (1)$$

where the decay width $\Gamma_{K\text{shell}}$ and $\Gamma_{p-\text{emit}}$ is the equivalent of $\hbar/\tau_{K\text{shell}}$ and $\hbar/\tau_{p-\text{emit}}$, respectively, as they both follow the exponential decay law. Because the K-shell vacancy lifetimes are well known both experimentally and theoretically, ranging from $\tau \approx 2\times10^{-15}$ s for carbon down to $\tau \approx 6\times10^{-18}$ s for uranium [2, 3], lifetimes of proton-emitting states can be established with reasonable accuracy. The preceding discussion is also generalizable to EC-delayed α-particle emission. This 'atomic clock' method has been successfully applied to measure the average sub-fs lifetimes of proton-unbound states populated by the ECs of ^{65}Ge [4], ^{69}Se [5, 4], ^{73}Kr [6, 7, 4], ^{77}Sr [4], ^{113}Xe [8], and ^{117}Ba [9].

In all the aforementioned cases, excited states could not be distinguished individually as their level density was too high, and none of the measured lifetimes were discussed in an astrophysical context. High-resolution measurements on γ rays and protons would enable refinement of the PXCT by introducing the possibility of selecting the initial proton-emitting state and the excited final state. We have buit a PXCT apparatus to extend this technique to constrain the lifetimes of resonances of interest for astrophysics.

2. Scientific Motivations

2.1. Application for rp-process

Type I X-ray bursts (XRBs) are the most frequent type of thermonuclear stellar explosions in the Galaxy. They are powered by thermonuclear runaways in hydrogen- and/or helium-rich material accreted onto the surface of a neutron star in a low-mass X-ray binary system. The main nuclear reaction flow in the XRB is driven toward the proton drip-line and to

*Corresponding author
Email address: wrede@frib.msu.edu (C. Wrede)

high masses via the αp-process (a sequence of (α, p) and (p, γ) reactions) and the rp-process (a series of rapid proton-captures and β^+-decays). Accurate nuclear physics inputs such as β decay rates, masses, and nuclear reaction rates of neutron-deficient rare isotopes along the path of the αp- and the rp-process are needed to model the energy production and nucleosynthesis in XRBs. Our understanding of XRBs has greatly expanded while they still hold many open questions despite decades of work [10, 11, 12].

In a recent investigation to identify important reaction rates that affect XRB observables and nucleosynthesis, the ^{59}Cu$(p,\gamma)^{60}$Zn and ^{59}Cu$(p,\alpha)^{56}$Ni reaction rates were predicted to have significant impacts on the modeling of X-ray burst light curves and the composition of the burst ashes [13]. Under XRB conditions, the reaction flux beyond ^{56}Ni is affected by several cycles. As indicated in Fig. 2, a low ^{59}Cu$(p,\gamma)^{60}$Zn or a high ^{59}Cu$(p,\alpha)^{56}$Ni rate leads to the formation of a stronger NiCu cycle that strongly limits the synthesis of heavier nuclei and also affects the light curves [14]. Proton-capture onto ^{59}Cu either returns the cycle to ^{56}Ni or breaks out via ^{59}Cu(p,γ), depending on the $(p,\gamma)/(p,\alpha)$ rate ratio. The critical quantity determining the strength of the NiCu cycle is the ratio of the (p,α) to (p,γ) reaction rates at ^{59}Cu.

For a narrow isolated resonance, the resonant reaction rate can be calculated using the well-known relation [15],

$$N_A\langle\sigma v\rangle_r = 1.5394\times10^{11}(\mu T_9)^{-3/2}\times\omega\gamma \times\exp\left(-\frac{11.605E_r}{T_9}\right)(\mathrm{cm^3 s^{-1} mol^{-1}}), \quad (2)$$

where $\mu = A_T/(A_p + A_T)$ is the reduced mass in atomic mass units, with $A_p = 1$ and $A_T = 59$ as the mass numbers of proton and ^{59}Cu, respectively. E_r is the resonance energy in the center-of-mass system in units of MeV. T_9 is the temperature in units of giga kelvin (GK), and $\omega\gamma$ is the resonance strength in units of MeV, which is defined as:

$$\omega\gamma = \frac{2J_r+1}{(2J_p+1)(2J_T+1)}\frac{\Gamma_p\times\Gamma_\gamma}{\Gamma_{\mathrm{tot}}}, \quad (3)$$

where J_r is the spin of the resonance, $J_p = 1/2$ is the spin of proton, and $J_T = 3/2^-$ is the spin of the ground state of ^{59}Cu. The total decay width Γ_{tot} of the resonance is the sum of its partial decay widths, i.e., proton width (Γ_p), γ width (Γ_γ), and α width (Γ_α) since they represent the three open decay channels for the resonances of relevance to the thermonuclear ^{59}Cu$(p,\gamma)^{60}$Zn reaction rate. Alternatively, the resonance strength can be constructed by combining the level lifetime τ and the proton branching ratio $B_p = \Gamma_p/\Gamma_{\mathrm{tot}}$ using the following expression:

$$\omega\gamma = \frac{2J_r+1}{(2J_p+1)(2J_T+1)}B_pB_\gamma\frac{\hbar}{\tau}, \quad (4)$$

which are also applicable to the ^{59}Cu$(p,\alpha)^{56}$Ni reaction by replacing the γ terms with α terms ($J_\alpha = 0$). Therefore, measurements of the proton, γ-ray, and α-decay branching ratios, and the lifetimes of the ^{60}Zn resonances within the Gamow window will suffice to determine the contribution of resonant charged-particle capture to the total reaction rates. Usually, we could use two techniques, β decay spectroscopy and the Doppler-shift attenuation method, and therefore, two separate experiments to measure branching ratios and lifetimes and constrain thermonuclear rates. Applying the PXCT based on EC is well suited to measure both in a single experiment.

The Gamow energies and windows for the ^{59}Cu$(p,\gamma)^{60}$Zn and ^{59}Cu$(p,\alpha)^{56}$Ni reactions shown in Table 1 are calculated from a numerical study of the relevant energy ranges for astrophysical reaction rates [16]. It can be seen that at any given temperature below 2 GK, the corresponding effective energy windows will not exceed 2.8 MeV. Combined with the proton-separation energy of ^{60}Zn $S_p(^{60}\mathrm{Zn}) = 5105.0(4)$ keV and α-separation energy of ^{60}Zn $S_\alpha(^{60}\mathrm{Zn}) = 2691.7(5)$ keV, the excitation energy of interest should be from 5.1 to 7.9 MeV. Therefore, the key resonances in ^{60}Zn are energetically accessible in the β decay of ^{60}Ga owing to the large $Q_{\mathrm{EC}}(^{60}\mathrm{Ga}) = 14580(200)$ keV. In a recent ^{58}Ni$(^3\mathrm{He},n)^{60}$Zn reaction measurement [17], the nuclear level density of ^{60}Zn was extracted from the neutron evaporation spectrum. For the excitation energies at 6 MeV, the level density is estimated to be only $\sim$18 MeV^{-1}. The β decay of the 2^+ ground state of ^{60}Ga preferentially populates $J^\pi = 1^+$, 2^+, and 3^+ states in ^{60}Zn according to the β-decay selection rules. As the $\ell = 1$ proton captures on the $3/2^-$ ^{59}Cu ground state populate ^{60}Zn 0^+, 1^+, 2^+, and 3^+ resonances, indicating an even lower level density for the states selected by β decay. All the ^{60}Zn states populated by allowed transitions are positive parity states, whereas the $\ell = 0, 2$ proton captures require a parity change. Based on our calculation, proton captures with $\ell = 0.2$ are less significant. It is expected to obtain the properties of the ^{60}Zn resonances by identifying the discrete states populated in the β-decay of ^{60}Ga (see Fig. 3).

To narrow down the important resonances, we performed shell-model calculations using the NuShellX@MSU code [18] in the full fp-shell model space with the GPFX1A interaction [19]. The properties of 72 ^{60}Zn states within excitation energies of 5 – 6.5 MeV are calculated and used as input to determine the resonant capture component of the ^{59}Cu$(p,\gamma)^{60}$Zn reaction rate. As shown in Table 2, the resonant capture contributions from four resonances are found to be dominant over a temperature range. A quenching factor $q^2 = 0.6$ for the matrix elements of the Gamow-Teller operator was used to calculate the β-feeding intensities in the ^{60}Ga decay. It can be seen that at least one of the four key resonances can be populated with a large decay branching ratio, and thus a lower limit on the ^{59}Cu$(p,\gamma)^{60}$Zn reaction rate would be set. A strong lower limit on the ^{59}Cu$(p,\gamma)^{60}$Zn reaction rate would indicate very weak NiCu cycling and therefore solve the astrophysical problem.

Even if the level density is still too high to distinguish discrete resonances, we can derive the particle and γ-transmission coefficients, which are essential ingredients to calculate the reaction rates with the statistical model [20]. Calculations in the statistical model require the input of a

Table 1: Gamow windows $\widetilde{E}_{\rm hi} - \widetilde{\Delta} \le E \le \widetilde{E}_{\rm hi}$ and Gamow peaks $\widetilde{E}_0$ for the ^{59}Cu$(p,\gamma)^{60}$Zn and ^{59}Cu$(p,\alpha)^{56}$Ni reactions at a temperature T.

	^{59}Cu$(p,\gamma)^{60}$Zn			^{59}Cu$(p,\alpha)^{56}$Ni		
T (GK)	$\widetilde{E}_{\rm hi} - \widetilde{\Delta}$ (MeV)	$\widetilde{E}_{\rm hi}$ (MeV)	$\widetilde{E}_0$ (MeV)	$\widetilde{E}_{\rm hi} - \widetilde{\Delta}$ (MeV)	$\widetilde{E}_{\rm hi}$ (MeV)	$\widetilde{E}_0$ (MeV)
0.5	0.51	0.92	0.71	0.55	0.98	0.74
1.0	0.67	1.26	0.91	0.73	1.48	1.01
1.5	0.75	1.57	1.01	0.87	2.11	1.27
2.0	0.82	1.83	1.14	1.01	2.80	1.74

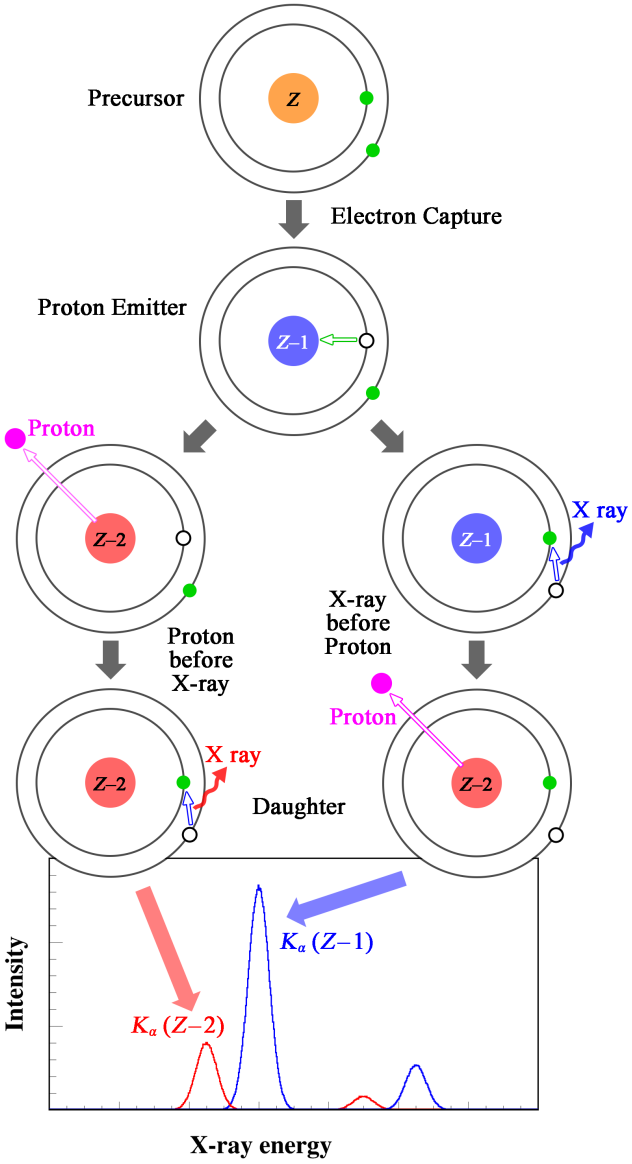

Figure 1: Cartoon illustrating the proton-X-ray coincidence technique. See text for details.

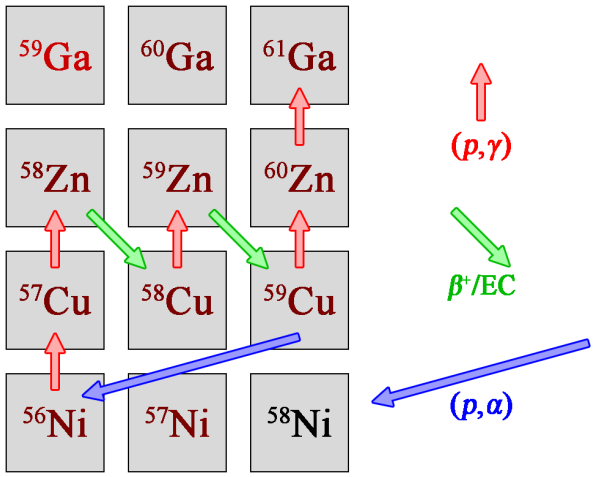

Figure 2: Portion of the *rp*-process reaction sequence featuring the NiCu reaction cycle.

Table 2: Properties of the dominant resonances in the ^{59}Cu$(p,\gamma)^{60}$Zn reaction. The values listed in the first through fifth columns are the dominating region of temperature, spin and parity (J^π), excitation energy (E^*), resonance energy (E_r), and β-feeding intensity (I_β) of each resonance, respectively.

T (GK)	J^π	E^* (keV)	E_r (keV)	I_β (%)
0.10 – 0.15	3^+	5362	257	0.05
0.15 – 0.45	1^+	5568	463	3.75
0.45 – 0.70	2^+	5648	543	0.15
0.70 – 7.50	2^+	6079	974	0.39

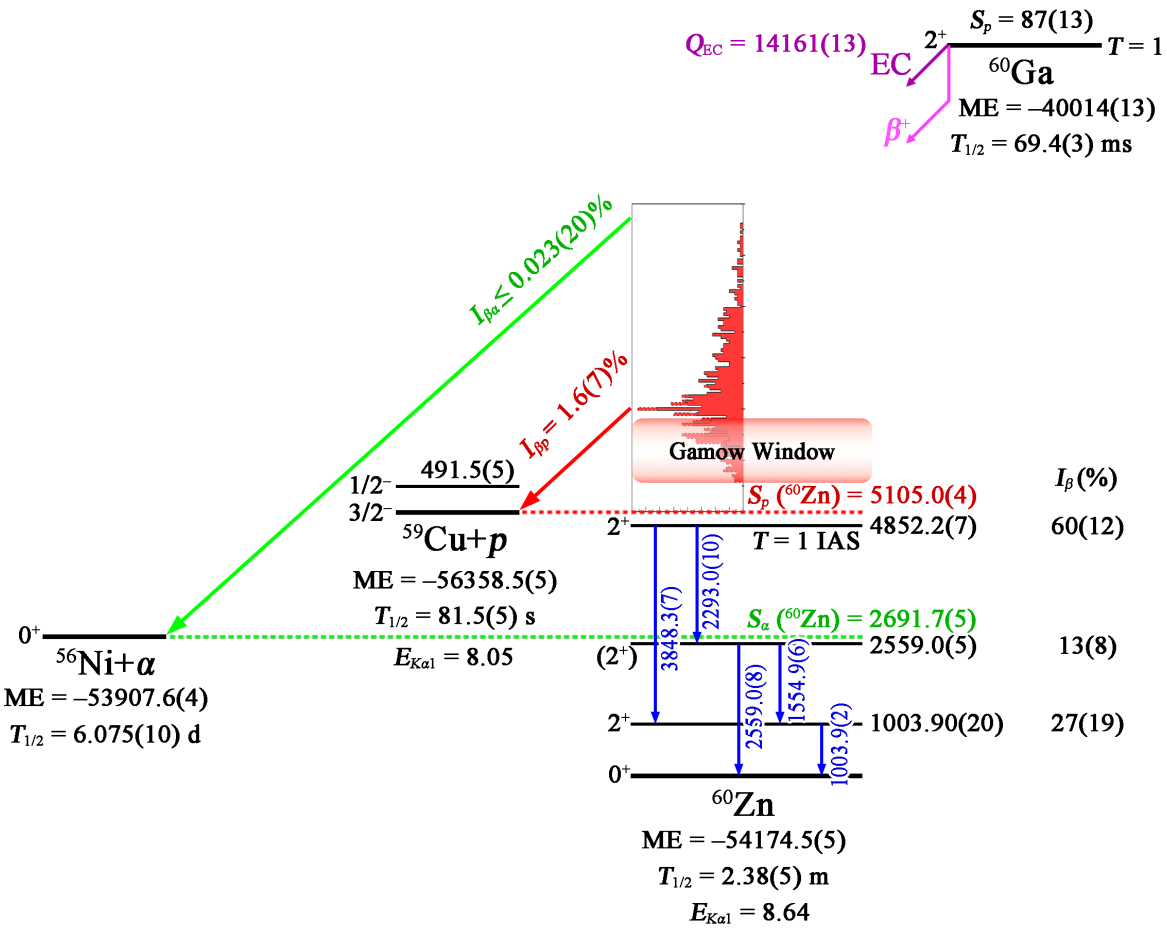

Figure 3: Previously established decay scheme of ^{60}Ga. All energies labeled in the scheme are given in units of keV. The mass excesses of ^{56}Ni, ^{59}Cu, and ^{60}Zn are from AME2020 [25]. The mass excess of ^{60}Ga is the weighted average of values reported by Refs. [26, 27]. The proton-separation energy and the β-decay Q-value of ^{60}Ga are obtained using this average mass. The spins, parities, and excitation energies are from the evaluation [28]. The γ-ray energies, β-feeding intensities, and the proton spectrum are from ^{60}Ga β spectroscopy of [29]. The half-life of ^{60}Ga is the weighted average of values reported by Refs. [26, 29, 30, 31].

number of different statistical properties. The standard approach in the calculation of reaction rates for astrophysics in a Hauser-Feshbach statistical model is to include a number of discrete excited states when experimentally known. The important ingredients of statistical model calculations are the particle and γ-transmission coefficients T and the level density of excited states ρ. Currently, experimental information on the ^{59}Cu$(p,\gamma)^{60}$Zn and ^{59}Cu$(p,\alpha)^{56}$Ni reactions is scarce. A direct cross section measurement of the ^{59}Cu$(p,\alpha)^{56}$Ni reaction at energies far higher than the Gamow window for X-ray bursts was found to be lower than statistical model calculations [21]. The PXCT approach has wide applicability to constrain other reaction rates of particular importance in the *rp*-process. As ^{64}Ge plays an analogous role in the ZnGa cycle to the role of ^{60}Zn in the NiCu cycle, it is desirable to extend this method to study the β-decay of ^{64}As in the future.

In addition to the lifetimes obtained from the measured K_α X-ray intensities, the system also measures proton, γ-ray, and α-particle branching ratios (Γ_p/Γ, Γ_γ/Γ, Γ_α/Γ, respectively), ideally for discrete resonances for the first time. By gating on different protons and γ rays, we can extract the lifetime for a specific state. This method will also provide experimental information on the nuclear level density and transmission coefficients needed to calculate rates using the statistical model. Based on a complete set of data, the ^{59}Cu$(p,\gamma)^{60}$Zn and ^{59}Cu$(p,\alpha)^{56}$Ni reaction rates will be constrained. Hence, the proposed work has the potential to make a major step toward addressing the unknown strength of the NiCu cycle, which is of critical importance for understanding the *rp*-process and the modeling of X-ray burst light curves.

The ^{60}Ga experiment cannot be run at TRIUMF-ISAC or CERN-ISOLDE because they cannot provide a ^{60}Ga beam of any intensity. The nearest isotope, ^{61}Ga, has only been produced at around 140 and 10 pps, respectively. FRIB will be the only facility in the world able to run the ^{60}Ga experiment in the foreseeable future. Considering a ^{60}Ga fast beam rate of 3.0×10^5 per second at FRIB, a week-long experiment would yield sufficient statistics using the built setup. To commission the PXCT setup in the D-line stopped-beam area of FRIB, we chose to reproduce the lifetimes obtained in the EC of ^{73}Kr (Fig. 4), one of the most well-studied cases by previous PXCT measurements [4, 6, 7] and decay spectroscopy [50]. Using the most recent version of LISE++ obtained from FRIB beam physicists including their "reality factor" yields a ^{73}Kr fast-beam intensity of 3.3×10^5 pps based on a ^{78}Kr primary beam incident upon a ^{12}C production target. Assuming an efficiency of 18.5% for extraction and delivery from the linear gas stopper based on the online FRIB beam-rate calculator yields 6.1×10^4 delivered to the implantation foil of the experimental setup.

2.2. *Application for p-process*

About 30−35 proton-rich nuclei, ranging from ^{74}Se to ^{196}Hg, the so-called *p* nuclei, cannot be produced by the *s* and *r* processes via neutron-capture reactions. The astrophysical origins of these nuclei are not yet fully understood. To date, the favored process for the production of *p*-nuclei has been the γ-process occurring in Type II Supernovae when the shock-front passes through the O- and Ne-rich layer of the star where temperatures are between $1.8 < T_9 < 3.3$ [22]. Currently, the γ-process nucleosynthesis calculations are mostly based on theoretical calculations of cross sections using the Hauser-Feshbach statistical model [32]. The nuclear statistical parameters that are required in such calculations are optical model potential, γ-ray strength functions, and nuclear level densities [23]. PXCT can also be applied to measure individual resonance strengths or to constrain the transmission coefficients of both the entrance and exit channels for statistical model calculations of thermonuclear rates.

Rauscher *et al.* performed a comprehensive, large-scale Monte Carlo study of nucleosynthesis in the γ process [33]. ^{110}Sn$(\gamma,p)^{109}$In is identified as one of the key rates determining the production uncertainties of *p*-nuclei ^{96}Ru and ^{106,108}Cd in the 15- and 25-M$_\odot$ KEPLER model. Rapp *et al.* investigated the reaction flux patterns of the *p*-process using a multimass zone Type II SN shock-front model [34]. The ^{110}Sn$(\gamma,p)^{109}$In and ^{110}Sn$(\gamma,\alpha)^{106}$Cd reactions are both identified as particularly important (Fig. 5). PXCT can be used to measure lifetimes and branching ratios of unbound ^{110}Sn states for proton, α, and γ emission by the EC decay of ^{110}Sb to ^{110}Sn, which can then decay by proton or α emission to ^{109}In and ^{106}Cd, respectively (Fig. 6). This will provide insights into the competition between the ^{110}Sn$(\gamma,p)^{109}$In and ^{110}Sn$(\gamma,\alpha)^{106}$Cd reactions in the astrophysical γ process.

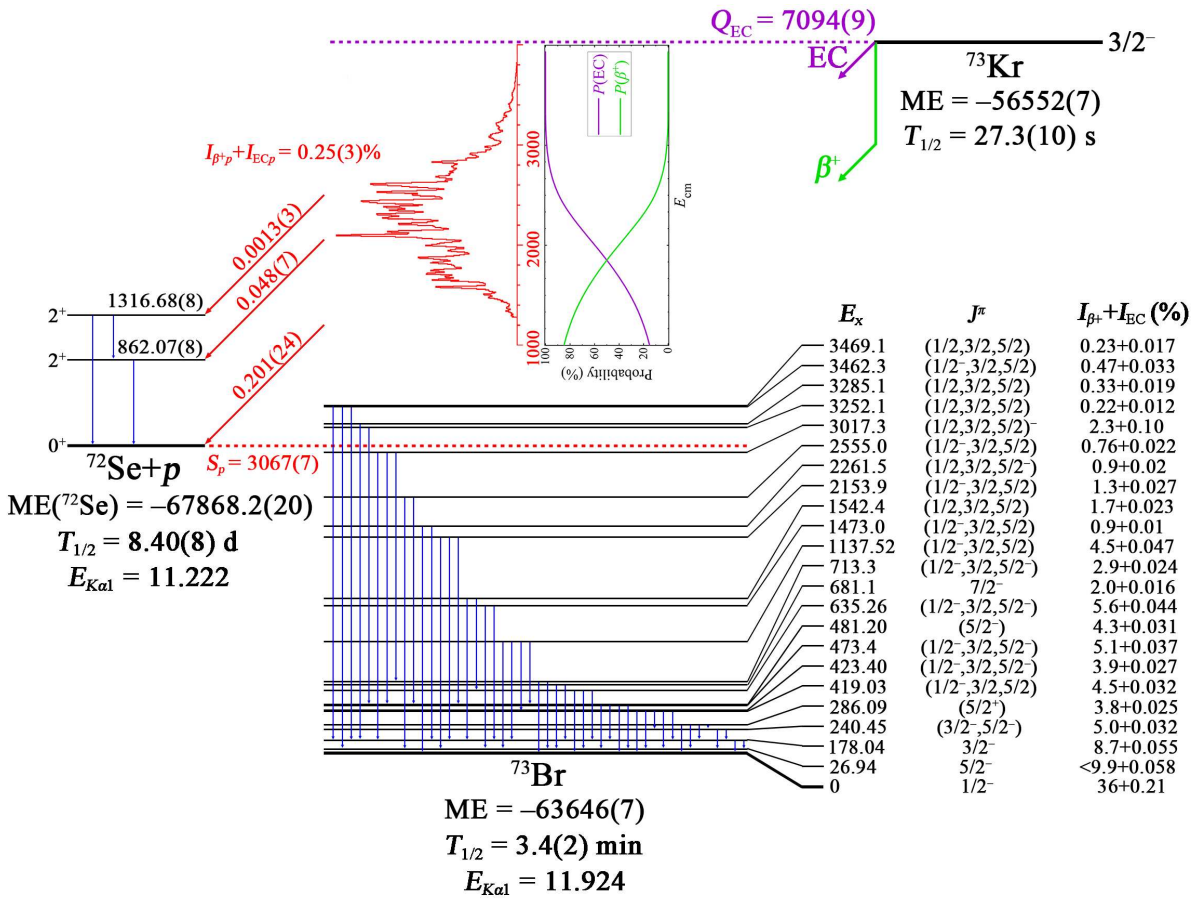

Figure 4: Previously established decay scheme of ^{73}Kr. All energies labeled in the scheme are given in units of keV. The mass excesses, the proton-separation energy, or the β-decay Q-value of ^{72}Se, ^{73}Br, and ^{73}Kr are from AME2020 [25]. All the half-lives and the spins, parities, excitation energies, and β-feeding intensities of ^{73}Br states are from the evaluation [49].

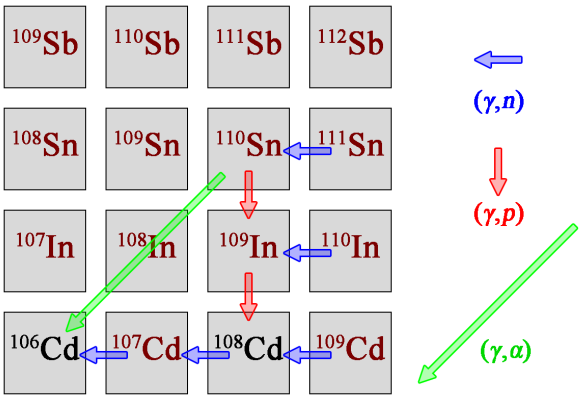

Figure 5: Portion of the *rp*-process reaction sequence featuring the NiCu reaction cycle.

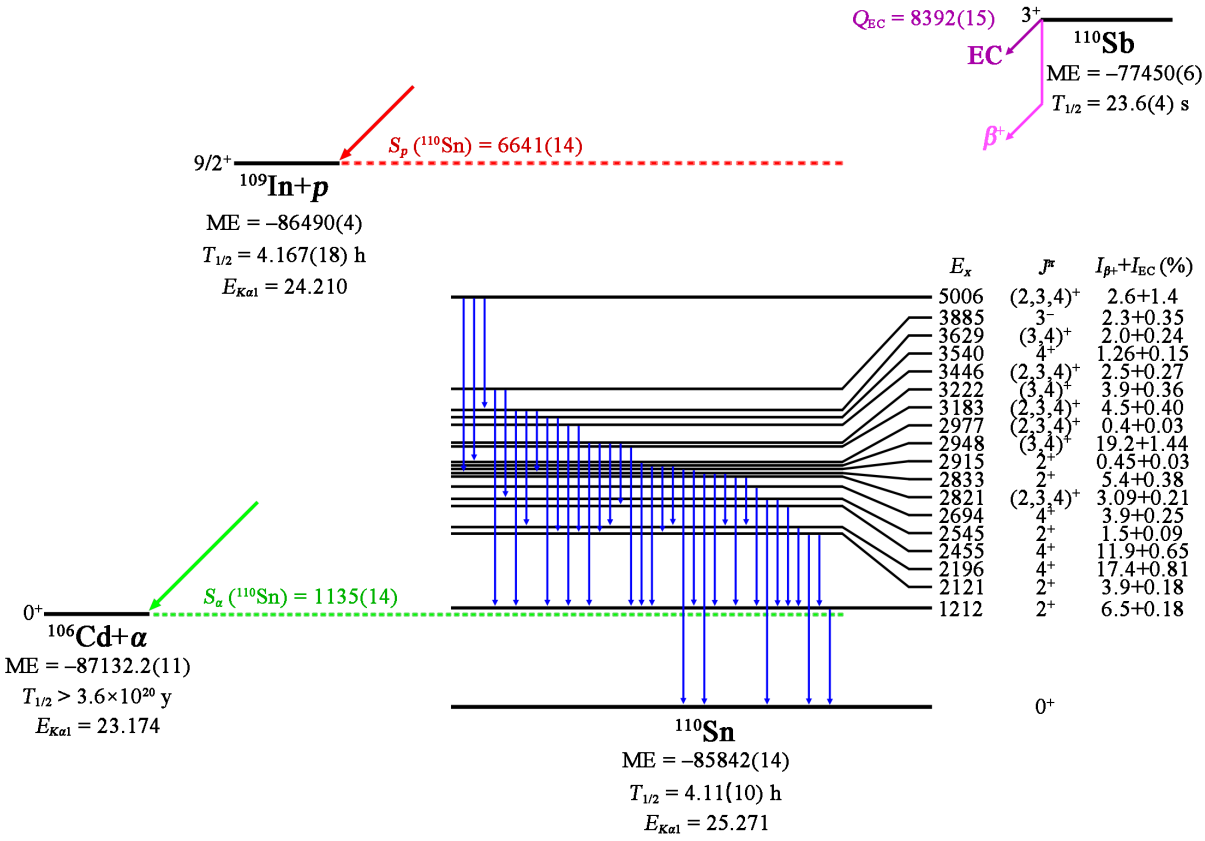

Figure 6: Previously established decay scheme of ^{110}Sb. All energies labeled in the scheme are given in units of keV. The mass excesses, the particle-separation energy, or the β-decay Q-value of ^{106}Cd, ^{109}In, ^{110}Sn, and ^{110}Sb are from AME2020 [25]. The spins, parities, excitation energies, and β-feeding intensities of ^{110}Sn states are from the evaluation [35]. The half-life of ^{110}Sb is the weighted average of values reported by Refs. [36, 37, 38].

3. Experimental Setup

We have built a PXCT detection system at the Facility for Rare Isotope Beams, where a sufficient intensity of the ^{60}Ga beam will enable the application of this technique to study the ^{60}Zn resonances populated in the EC decay of ^{60}Ga [29]. The configuration of the PXCT apparatus is presented in Fig. 7. The beam is implanted into a thin carbon collection foil at the center of a vacuum chamber. The detection system comprises a ΔE-E silicon detector telescope for charged-particle detection, two large-volume coaxial germanium detectors for γ-ray detection, and a planar germanium detector for X-ray detection. To mitigate the attenuation of X-rays, we employ thermalized beams because of their shorter implantation depths compared with fast beams.

3.1. Detectors

We have selected two circular Si detectors, MSD12 of 12 μm thickness [39] and MSD26 of 1000 μm thickness [40] manufactured by Micron Semiconductor Ltd to construct the ΔE-E telescope. The numbers following MSD indicate the active area diameter in millimeters. The dead layer window and metallization type for MSD12 are 9.5P/7P, and for MSD26 are 9.5P/2M. Here, 9.5 represents a boron-doped silicon dead layer with a thickness of 50 nm, 7 represents a dead layer with a thickness of 300 nm, and 2 represents a dead layer with a thickness of 500 nm. P denotes a periphery metal band with a width of 30 μm around the edge of the active areas and contact pads for wire bonding and the majority of the active area does not have metal coverage. M denotes a continuous aluminum coverage with a thickness of 500 nm over the entire active area region. Both silicon chips are assembled onto an FR4 printed circuit board.

We have selected a Mirion Low Energy Germanium Detector (LEGe) model GL0510 (S/N:13725) for X-ray detection [41]. The LEGe detector consists of a Ge crystal with a diameter of 25.0 mm and a length of 10.5 mm. LEGe is housed in a cryostat with a diameter of 38.1 mm and a 0.13-mm thick beryllium entrance window, ideally suited for X-ray spectroscopy from 3 keV up. LEGe is fabricated with a thin contact on the front face and a rear contact that covers less than the full area, resulting in lower capacitance compared to a planar device of similar size. Since preamplifier noise is a function of detector capacitance, LEGe features low noise and high resolution at low and moderate energies.

We have selected two Mirion Extended Range Coaxial Germanium Detectors (XtRa) model GX10020 for γ-ray detection [42]. The active volume of XtRa1 (S/N:5593) has a diameter of 84.8 mm and a thickness of 65.2 mm, while XtRa2 (S/N:5596) has a diameter of 79.8 mm and a thickness of 80.0 mm. Conventional coaxial detectors have a lithium-diffused contact typically of 0.5 to 1.5 mm thickness, which forms a dead layer that stops most photons below 40 keV, rendering the detector virtually inefficient at low energies. However, the XtRa detectors, feature an exclusive thin window contact on the front surface and a 0.6-mm-thick carbon composite cryostat window, which enables a good low-energy response.

All three Ge detectors are equipped with the Cryo-Pulse 5 Plus (CP5-Plus) electrically refrigerated cryostat. A 5-watt pulse tube cooler is integrated into a compact coldhead-assembly, which is directly attached to the detector housing. CP5-Plus features low vibration, low noise, low power demand, and a maintenance-free operation [43]. The assembly is connected to a bench-top power controller that provides the required output voltage to drive the compressor. The controller also contains the necessary logic to ensure the safe and reliable operation of the cryostat. An RS-232 serial interface and CP 5-Plus control panel application are also included, allowing for remote monitoring of the cooler status.

All three Ge detectors are equipped with the Intelligent Preamplifier (iPA) [44], which incorporates a low-noise field-effect transistor (FET) input circuit optimized for the ultra-high source impedance of germanium detectors. The first stage of iPA serves as an integrator providing an output voltage proportional to the accumulated charge from the detector, and also functions as an electrometer for measuring the leakage current of the detector. The second stage acts as an output buffer and allows for four conversion factors of 50, 100, 250, and 500 mV/MeV. The iPA generates an inverted output signal that is split into two outputs, each with a termination impedance of 93 and 50 Ω. Additionally, the iPA is equipped with a warm-up sensor that is thermally connected to the detector. A USB interface and a control panel application provide real-time monitoring of detector current, temperatures, and preamplifier operating voltages. The four output gains as well as external or internal test pulsers are selectable via the control panel application.

Both the Ge detector and the coldhead are equipped with temperature sensors that serve as safety measures. In the event that the temperature exceeds the normal operating range, these sensors trigger the high-voltage inhibit signal from the preamplifier and the controller, respectively. This feature ensures the timely shutdown of the high-voltage bias supply, providing protection to the detector.

3.2. Electronics

All the preamplifiers are powered by two MNV-4 NIM power distribution and control modules. A Mesytec MHV 4-channel bias supply module is used to provide the bias voltages to the two MSD Si detectors. MSD12 has a depletion voltage of 1.5 V and is operated at 3.0 V, and MSD26 has a 90-V depletion voltage and is operated at 130 V. We apply a negative bias to the p^+ contacts of both MSD detectors through MPR-1 charge-sensitive preamplifiers and the n^+ contacts are grounded. MHV offers a ramp speed as low as 5 V/s to protect the circuits of preamplifiers. MSD26 has a leakage current ranging from 55 to 100 nA, whereas MSD12 maintains a leakage current below 1 nA. Two ORTEC 660 Dual Bias Supply modules are used to provide bias voltages to the three Ge detectors. We apply a negative bias to the p+ contacts of LEGe and a positive bias to the n+ contacts of XtRa. LEGe becomes fully depleted at 600 V and is recommended to be

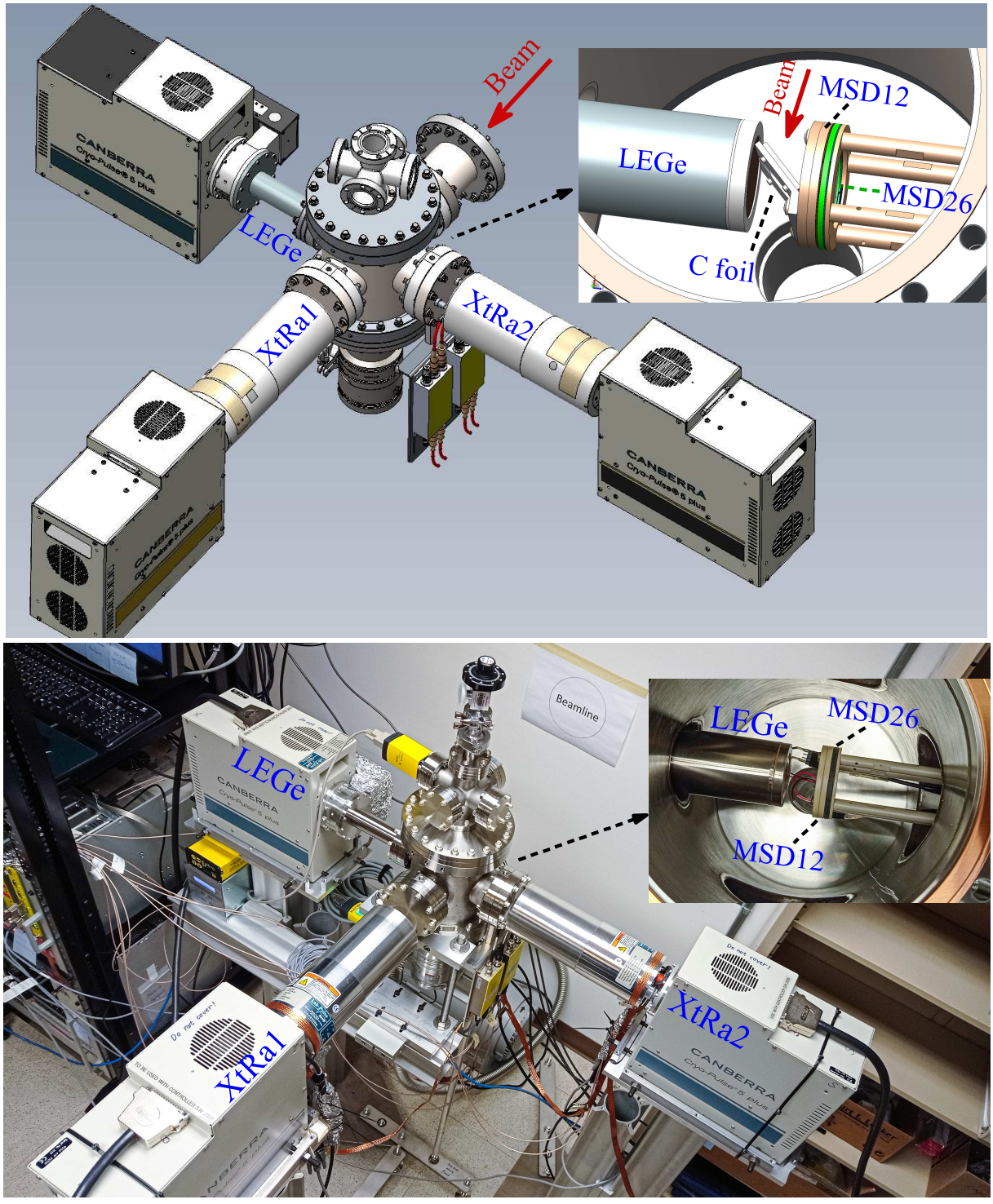

Figure 7: Mechanical design drawing and photograph of the PXCT detection system. The setup inside the vacuum chamber is highlighted in the insets.

operated at 1100 V. XtRa1 and XtRa2 become fully depleted at a bias voltage of +4000 V and +2200 V, respectively, and both operate at 4500 V. ORTEC 660 includes a remote bias shutdown feature to protect the preamplifier FET against damage in the instance of accidental warm-up of the Ge detector. The typical leakage currents of the two XtRa detectors are below 20 pA and below 100 pA for LEGe.

The tail pulses from MPR-1 exhibit rise times of 400-600 ns (MSD12) and 70 ns (MSD26), with a 120 μs decay constant. The tail pulses from iPA exhibit rise times of 150 ns (LEGe) and 250 ns (XtRa), with a 50 μs decay constant. The preamplifiers produce output signals with a 50 Ω impedance. These signals are transmitted via double-shielded RG316 coaxial cables of equal length and then digitized by a 16-bit, 250 Mega samples per second Pixie-16 module manufactured by XIA LLC [45]. The input impedance of each channel in Pixie-16 is configured to be 1 kΩ. A general-purpose nuclear physics data acquisition system Digital Data Acquisition System (DDAS) is used [51, 52] for recording and processing data. Trapezoidal filtering algorithms are implemented in both the slow filter for pulse height measurement and the fast filter for leading-edge triggering. Each event is timestamped using a constant-fraction discriminator (CFD) algorithm based on the faster filter response. Filter parameters are optimized according to Refs. [46, 53].

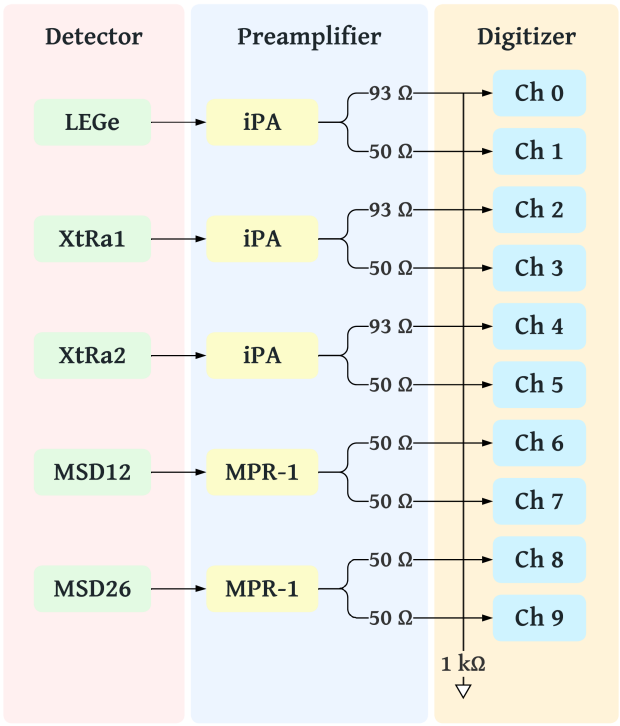

Figure 8: Schematic diagram of the electronics setup.

4. Performance Tests

We have performed comprehensive tests on the PXCT system, using the test configuration illustrated in Fig. 8 .

4.1. X-ray measurements

We have evaluated the performance of LEGe using the X rays and low-energy γ rays from ^{55}Fe, ^{152}Eu, and ^{241}Am radioactive sources, as shown in Fig. 9. The overall energy resolution achieved by LEGe is characterized by fitting the well-known X-ray or γ-ray lines with an exponentially modified Gaussian (EMG) function [47, 48] at 5.90 keV (Mn $K_{\alpha 1}$), 6.49 keV (Mn $K_{\beta 1}$), 11.89 keV (Np L_{ℓ}), 13.76 keV (Np $L_{\alpha 2}$), 13.95 keV (Np $L_{\alpha 1}$), 26.34 keV (^{237}Np γ), 33.20 keV (^{237}Np γ), 39.52 keV (Sm $K_{\alpha 2}$), 40.12 keV (Sm $K_{\alpha 1}$), 45.29 keV (Sm $K_{\beta 3}$), 45.41 keV (Sm $K_{\beta 1}$), and 59.54 keV (^{237}Np γ). At the energies of interest, 8.05 keV (Cu $K_{\alpha 1}$) and 8.64 keV (Zn $K_{\alpha 1}$), the full width at half maximum is estimated to be 238(8) and 241(7) eV, respectively, providing enough resolving power to distinguish between the characteristic X rays of the proton emitter and the daughter.

For photons below 100 keV interacting with Ge, the photoelectric effect is predominant, i.e., the photon is absorbed and its energy is transferred to an electron and causes prompt emission of a characteristic X ray as the resulting vacancy in the electron shell is filled. In most cases, this X ray is reabsorbed near the original interaction site. However, if the absorption occurs near the surface of Ge where the escape of the X ray can be significant, it results in peaks usually at 9.89 keV and 10.98 keV below the photopeaks, known as the Ge escape peaks (Fig. 9). These energy differences correspond to the characteristic $K_{\alpha 1}$ and $K_{\beta 1}$ X-ray energies for Ge, respectively [54].

For photon energies just above the K-shell binding energy of Ge, 11103.0 ± 2.0 eV [54], the incident photon is strongly absorbed without deep penetration beyond the detector surface. The subsequent characteristic K X ray tends to escape, thereby decreasing the full energy peak efficiency. This phenomenon can potentially complicate the normalization of near-edge X-rays. However, for our energies of interest in the range of 8-9 keV, K-shell absorption is no longer possible, and L-shell interactions dominate. In this case, incident gamma rays tend to penetrate somewhat deeper, and the energy of the fluorescent L X-ray is much lower, resulting in a reduced probability of escape.

4.2. γ-ray measurements

Figure 10 shows the γ-ray spectra measured by XtRa1 and XtRa2 using an ^{152}Eu source placed in the atmosphere and at the center of the vacuum chamber, respectively. It should be noted that in the latter case, the flanges between the source and XtRa are of 3.175-mm thickness, resulting in attenuation of x rays (Fig. 11). XtRa1 and XtRa2 have an absolute photopeak efficiency of 0.340(3)% and 0.322(3)% at 1 MeV, respectively. The error bars for the data points are given by the uncertainty of the γ-ray yields and the source activity. The activity of the ^{152}Eu calibration source is quoted with 1.4% accuracy by the manufacturer [55].

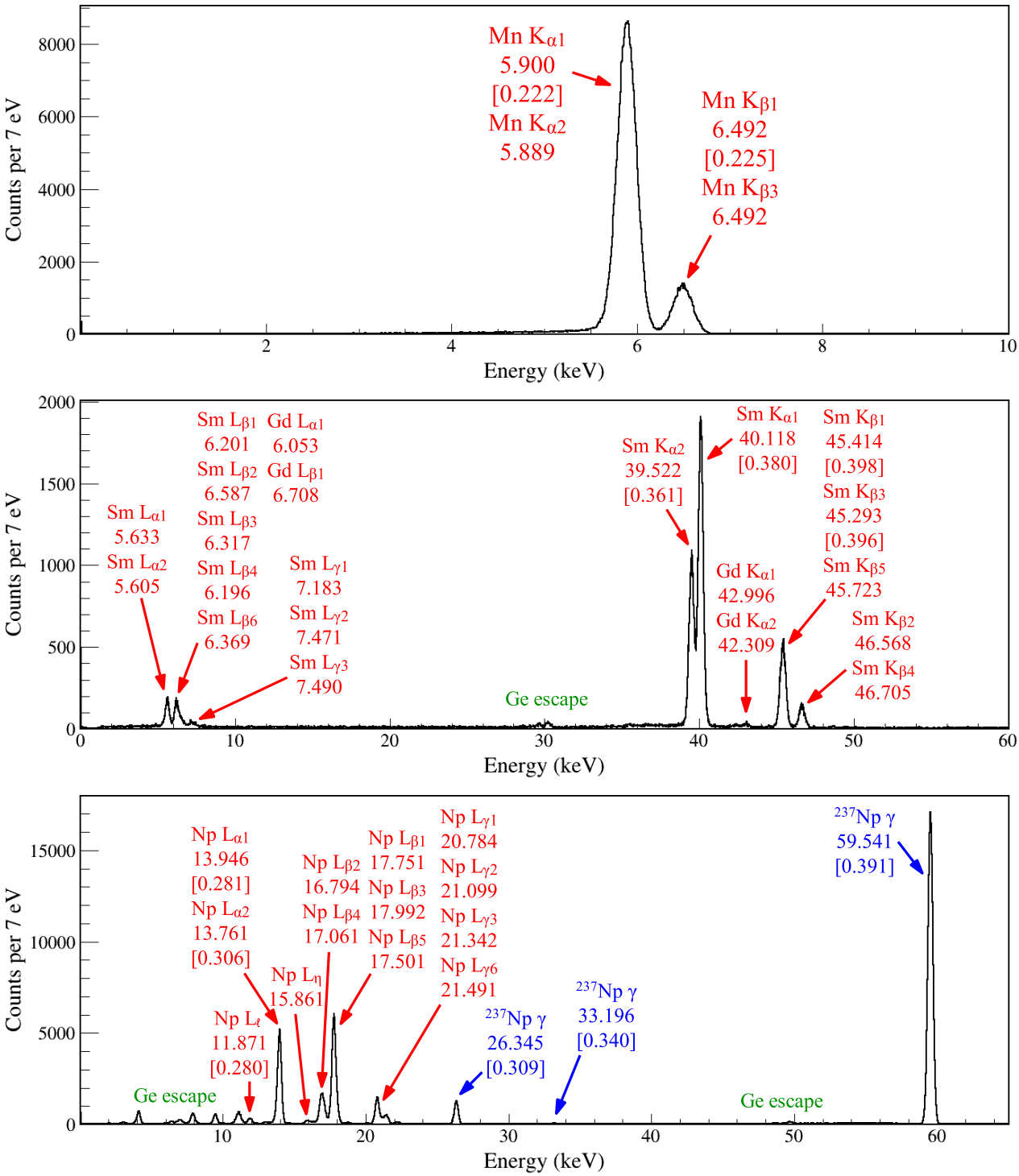

Figure 9: X-ray and/or γ-ray spectra measured by the LEGe detector using ^{55}Fe (top), ^{152}Eu (middle), and ^{241}Am (bottom) sources. All the X-ray energy values are adopted from Ref. [54] rounded to the nearest 0.01 keV. All the γ-ray energy values are adopted from Ref. [56] rounded to the nearest 0.01 keV. The FWHM values used to characterize the energy resolution of LEGe are indicated within brackets.

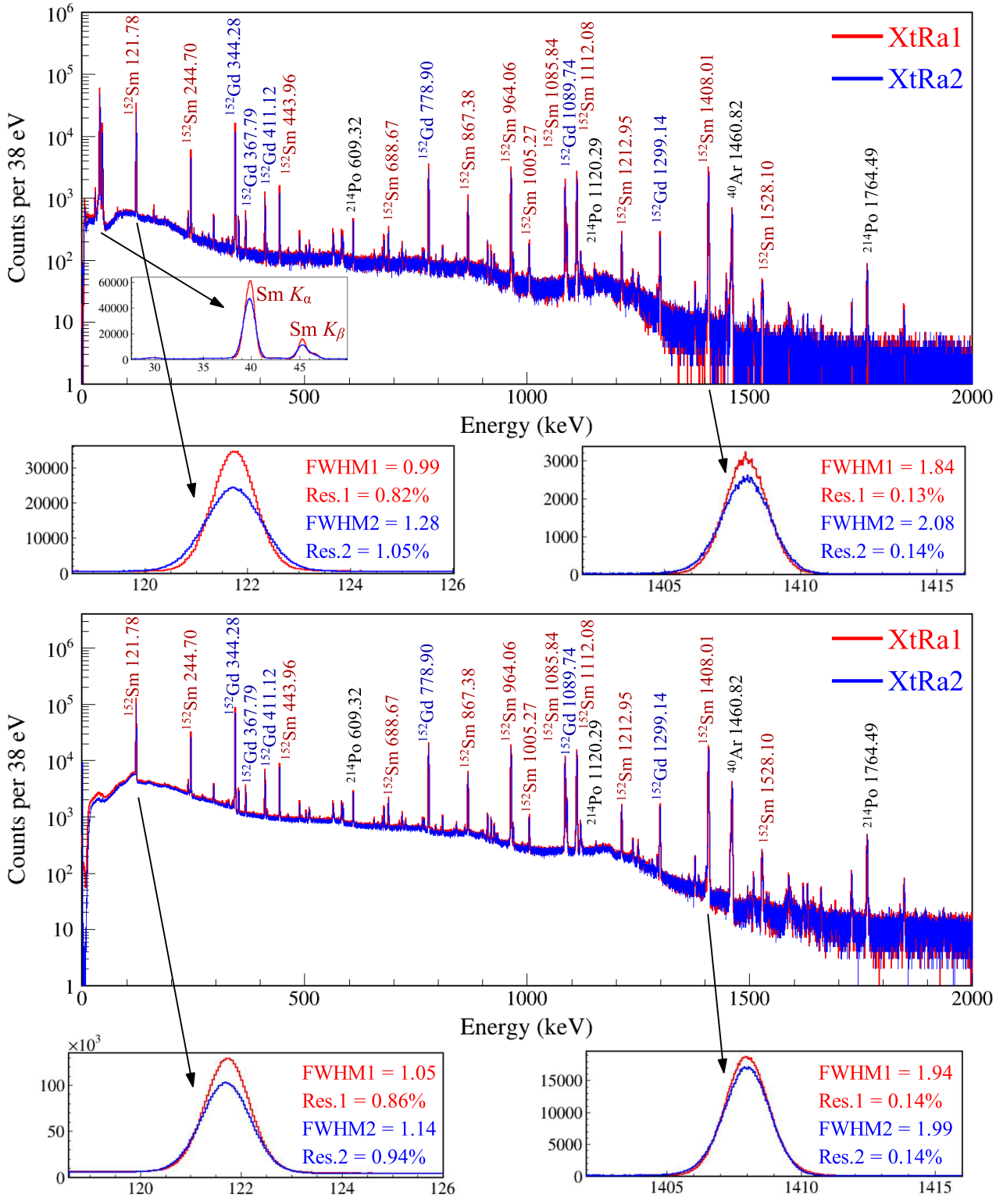

Figure 10: γ-ray spectra measured by XtRa1 (red) and XtRa2 (blue) using an ^{152}Eu source. Upper panel: ^{152}Eu source is placed in the atmosphere at a distance of 14 cm from the detector window. Lower panel: ^{152}Eu source is placed at the center of the vacuum chamber. All the γ-ray energy values are adopted from Ref. [57] rounded to the nearest 0.01 keV. The insets show the detector responses at 122 keV and 1408 keV. (For interpretation of the references to color in this figure caption, the reader is referred to the web version of this paper.)

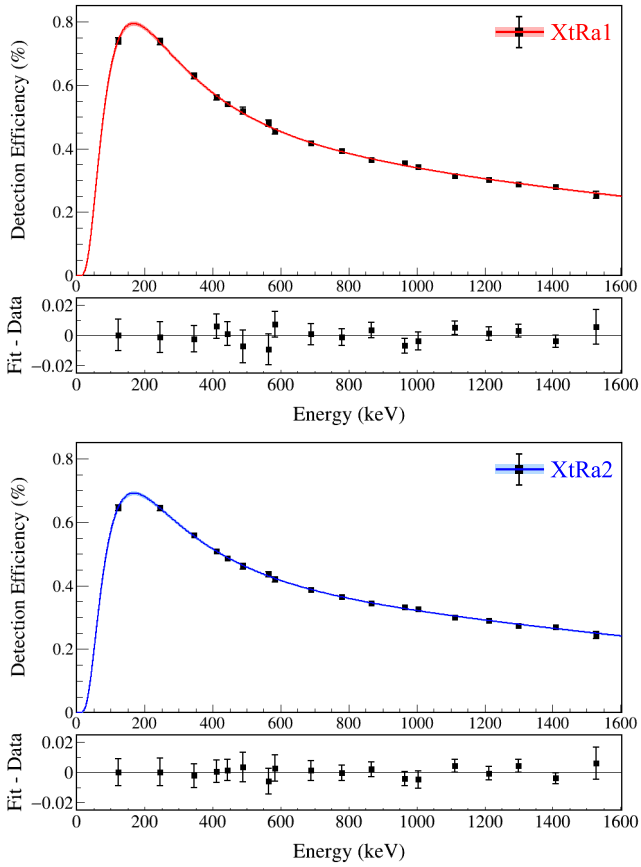

Figure 11: Absolute full-energy γ-ray detection efficiency of XtRas obtained using an ^{152}Eu source placed at the center of the chamber. The efficiency curves are fit using an exponential function that contains a polynomial of order 6 with the natural log of the energy.

4.3. α-particle measurements

Figure 12 shows the single α spectrum measured by MSD26 using an ^{241}Am source. Figure 13 shows the ΔE-E α spectrum measured by the telescope formed by MSD12 and MSD26. The α sum peak exhibits a resolution of 0.95%. In the ^{60}Ga experiment, the telescope will also be used to detect protons, which is anticipated to provide a higher resolution compared to that of α's. Using the ^{148}Gd and ^{241}Am sources, we calibrated MSD26 and measured the residual energy of ^{241}Am α particles in MSD26 with MSD12 installed in front of it. This allowed us to accurately determine the effective thickness of MSD12 to be 11.65(8) μm. Taking into account the thickness of 350 nm of the 9.5P/7P window, it brought the total thickness to a value that is consistent with the nominal value of 12 μm given in the Micron datasheet.

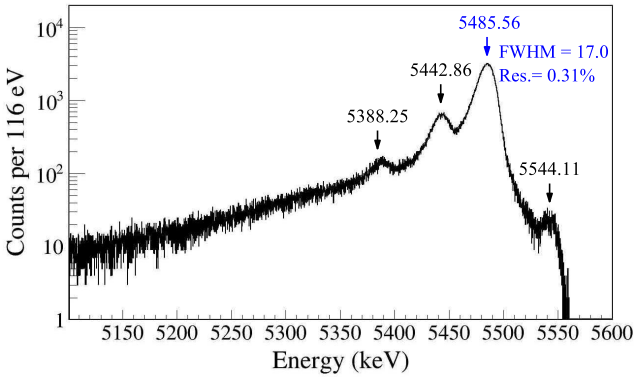

Figure 12: α spectrum measured by MSD26 using an ^{241}Am source. The α energy values are adopted from Ref. [58] rounded to the nearest 0.01 keV.

4.4. Coincidence measurements

Figure 14 shows the α-γ coincidence spectrum between the MSD detector telescope and LEGe obtained using an ^{241}Am source. The majority of low-energy photons emitted from ^{241}Am are effectively blocked by the source substrate, leaving only the 59.54-keV γ ray and its escape peaks noticeable. In all of these measurements, the ^{241}Am source is placed at the center of the chamber, 12 mm away from MSD12 and 10 mm away from the entrance window of LEGe.

Figure 15 shows parts of the γ spectrum measured by XtRa1 gated by the Sm K_α X rays measured by LEGe obtained using an ^{152}Eu source placed at the center of the chamber. By applying this coincidence condition, both the room background γ-ray lines and the β^--delayed γ ray lines from ^{152}Gd are substantially suppressed, which in turn, facilitates the identification of each γ-ray lines. What is left in the gated spectrum is purely EC-delayed γ rays from ^{152}Sm.

4.5. Timing performance

The timing performance of electronics was tested using a Canberra Model 1407P pulse generator. The generated pulse was fed to each test input of preamplifiers. The FWHM timing resolutions are estimated to be 0.32 ns (pulser), 37.4 ns

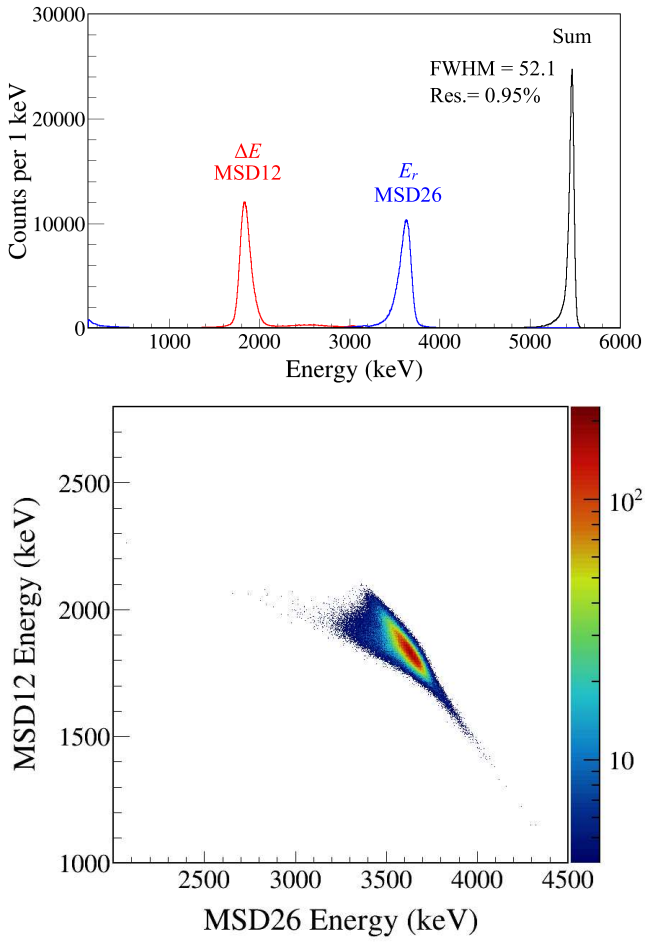

Figure 13: α spectrum measured by MSD12 and MSD26 using an ^{241}Am source. Upper: α-energy spectrum. Lower: ΔE-E 2D plot.

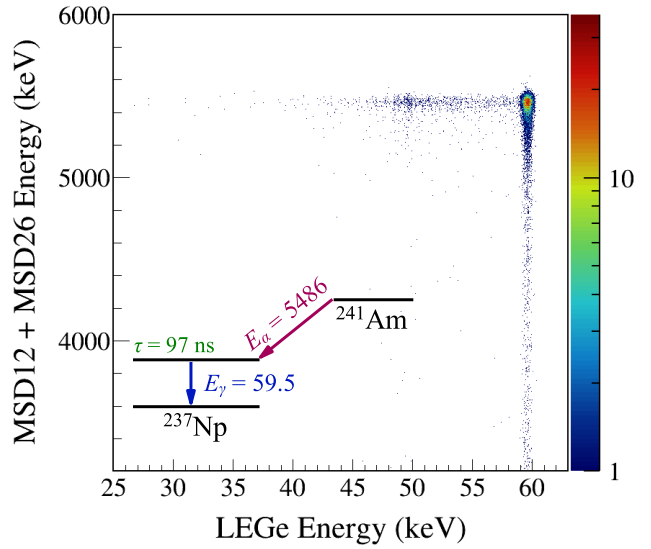

Figure 14: Coincidence spectrum between the MSD detector telescope and LEGe obtained using an ^{241}Am source placed at the center of the chamber. A simplified ^{241}Am decay scheme shows the dominant α-γ coincidence.

(MSD12), 4.4 ns (MSD26), 1.2 ns (XtRa1), and 1.8 ns (XtRa2). The amplitude resolutions obtained from the pulse test are 0.13% (Pulser), 3.17% (MSD12), 0.84% (MSD26), 0.26% (XtRa1), and 0.24% (XtRa2), demonstrating the electronic noise level present in the system. The timing performance of each detector was also studied using an ^{241}Am source placed at the center of the chamber and a ^{152}Eu source placed outside of the chamber (See Fig. 16). The sources were positioned in such a way that the α-γ coincidences could be measured by MSD ΔE-E and LEGe, and γ-γ coincidences could be measured by LEGe and two XtRa detectors. A 3-μs event window is applied for these measurements, which is large enough to include all the true coincidences and part of the accidental coincidences for subsequent subtraction. In the offline analysis, the coincidences between photons and charged particles can be established based on their relative time interval distributions.

Figure 17 shows the α-γ time difference distribution constructed by the start timestamps from α measured by the two MSDs stop timestamps from the 59.54-keV γ ray deexciting the 59.54-keV state in ^{237}Np measured by LEGe. By fitting the distribution with a function composed of exponential decay and a constant background, we obtained the half-life of the 59.54-keV excited state in ^{237}Np to be 67.99(18) ns. This value is consistent with the recent literature values of 67.86(9) ns [60] and 67.60(25) ns [59]. The statistical uncertainty was directly derived from the fitting program.

Two factors limit the time resolution that can be achieved with semiconductor detectors. Firstly, the charge collection process is inherently slow, typically taking several hundred nanoseconds. This time is much longer than the output from scintillators, making it hard to achieve the same level of time performance. Secondly, the shape of the pulse rise from semiconductor detectors can vary considerably from event to event, resulting in a wide range of leading-edge pulse shapes.

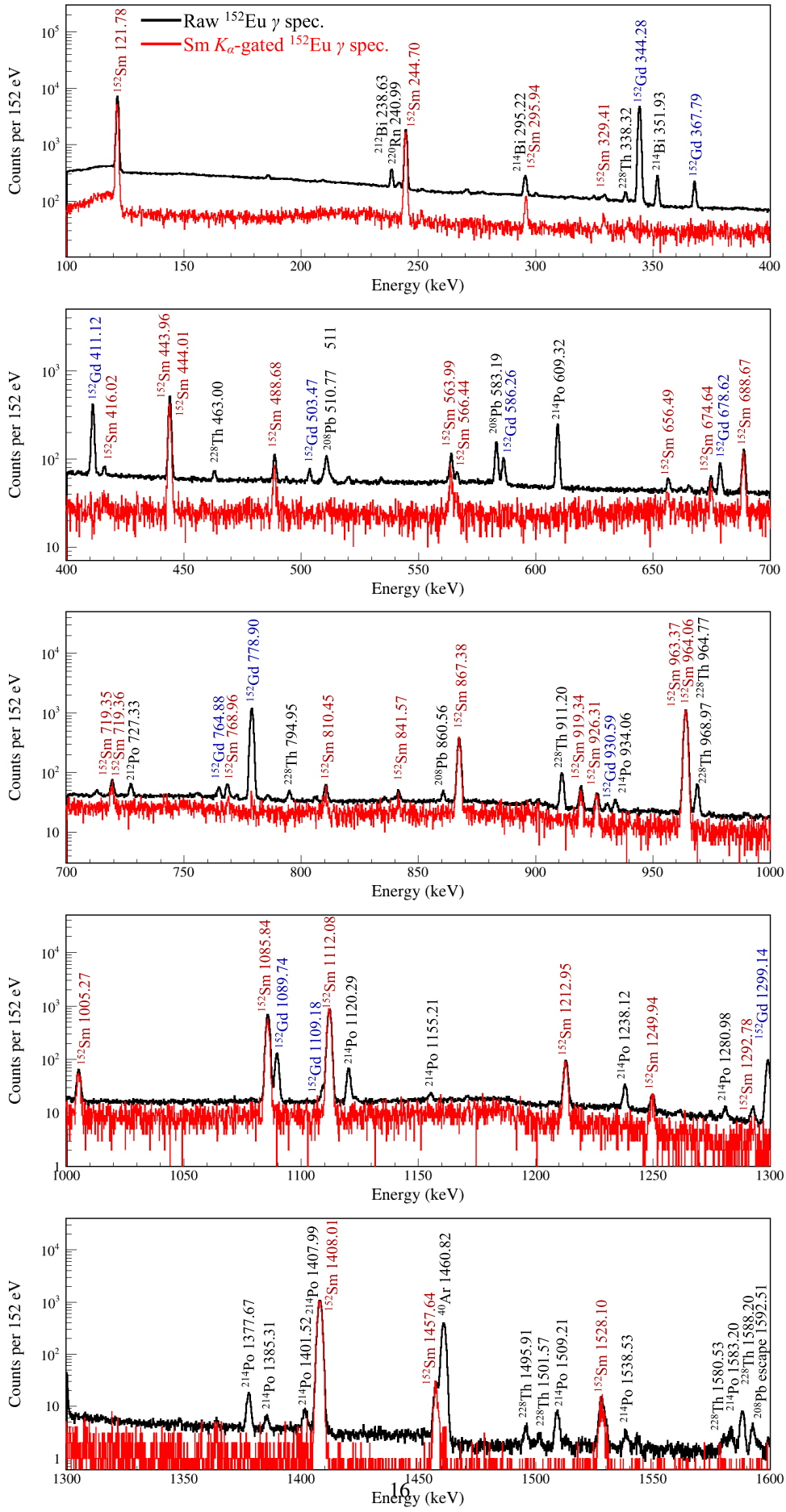

Figure 15: Black represents the raw γ-ray spectrum measured by XtRa1 using an ^{152}Eu source placed at the center of the chamber. Red represents γ-ray spectra gated by the Sm K_α X rays measured by LEGe. The raw spectrum is scaled down by a factor of 20 for better comparison.

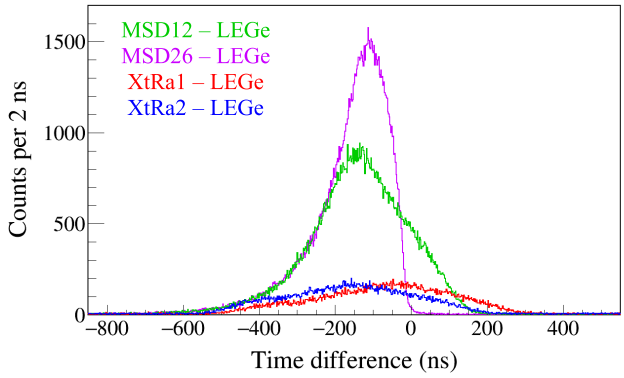

Figure 16: Coincidence time spectra between each detector obtained using an ^{241}Am source placed at the center of the chamber and a ^{152}Eu source placed outside of the chamber. The timestamps of the LEGe signals serve as the reference for the other four detectors.

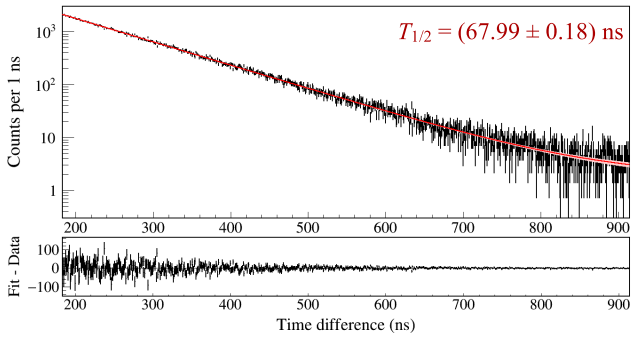

Figure 17: Time differences between the 59.54-keV γ-ray signals in LEGe and α signals in the MSD silicon detector telescope.

5. Summary

We aim to use a full-intensity ^{60}Ga FRIB beam to investigate ^{60}Zn resonances that determine the competition between the ^{59}Cu$(p,\gamma)^{60}$Zn and ^{59}Cu$(p,\alpha)^{56}$Ni reactions of the *rp* process in X-ray Bursts. This competition determines whether the so-called NiCu cycle is open or closed and therefore affects the shape of the observed light curve.

6. Acknowledgements

This work was supported by the National Science Foundation (USA) under Grants No. PHY-1419765, No. PHY-1404442, No. PHY-1430152, No. PHY-1565546, No. PHY-1913554, and PHY-2209429, and No. the US Department of Energy, Office of Science, under Award No. DE-SC0016052, Contract No. DE-AC05-00OR22725, and the US Department of Energy National Nuclear Security Administration under Awards No. DE-NA0003221 and No. DE-NA0000979.

References

[1] J. C. Hardy, J. A. Macdonald, H. Schmeing, H. R. Andrews, J. S. Geiger, R. L. Graham, T. Faestermann, E. T. H. Clifford, and K. P. Jackson, Phys. Rev. Lett. **37**, 133 (1976).
[2] J. H. Scofield, *Atomic Inner-Shell Processes* (Academic Press: New York (NY), USA, 1975).
[3] W. Bambynek, B. Crasemann, R. W. Fink, H. U. Freund, H. Mark, C. D. Swift, R. E. Price, and P. Venugopala Rao, Rev. Mod. Phys. **44**, 716 (1972).
[4] J. Giovinazzo, Ph. Dessagne, and Ch. Miehé, Nucl. Phys. A **674**, 394 (2000).
[5] J. A. Macdonald, J. C. Hardy, H. Schmeing, T. Faestermann, H. R. Andrews, J. S. Geiger, R. L. Graham, and K. P. Jackson, Nucl. Phys. A **288**, 1 (1977).
[6] P. Asboe-Hansen, E. Hagberg, P. G. Hansen, J. C. Hardy, P. Hornshøj, B. Jonson, S. Mattsson, P. Tidemand-Petersson, Phys. Lett. B **77**, 363 (1978).
[7] P. Asboe-Hansen, E. Hagberg, P. G. Hansen, J. C. Hardy, B. Jonson, and S. Mattsson, Nucl. Phys. A **361**, 23 (1981).
[8] Z. Janas, L. Batist, R. Borcea, J. Döring, M. Gierlik, M. Karny, R. Kirchner, M. La Commara, S. Mandal, C. Mazzocchi, F. Moroz, S. Orlov, A. Płochocki, E. Roeckl, and J. Żylicz, Eur. Phys. J. A **24**, 205 (2005).
[9] Z. Janas, L. Batist, J. Döring, M. Gierlik, R. Kirchner, J. Kurcewicz, H. Mahmud, C. Mazzocchi, A. Płochocki, E. Roeckl, K. Schmidt, P. J. Woods, and J. Żylicz, Eur. Phys. J. A **23**, 401 (2005).
[10] J. José, *Stellar Explosions: Hydrodynamics and Nucleosynthesis* (CRC/Taylor and Francis: Boca Raton (FL), USA, 2016).
[11] H. Schatz and K. E. Rehm, Nucl. Phys. A **777**, 601 (2006).
[12] A. Parikh, J. José, G. Sala, and C. Iliadis, Prog. Part. Nucl. Phys. **69**, 225 (2013).
[13] R. H. Cyburt, A. M. Amthor, A. Heger, E. Johnson, L. Keek, Z. Meisel, H. Schatz, and K. Smith, Astrophys. J. **830**, 55 (2016).
[14] L. van Wormer, J. Görres, C. Iliadis, M. Wiescher, and F.-K. Thielemann, Astrophys. J. **432**, 326 (1994).
[15] C. E. Rolfs and W. S. Rodney, *Cauldrons in the Cosmos* (University of Chicago, Chicago, 1988).
[16] T. Rauscher, Phys. Rev. C **81**, 045807 (2010).
[17] D. Soltesz, M. A. A. Mamun, A. V. Voinov, Z. Meisel, B. A. Brown, C. R. Brune, S. M. Grimes, H. Hadizadeh, M. Hornish, T. N. Massey, J. E. O'Donnell, and W. E. Ormand, Phys. Rev. C **103**, 015802 (2021).
[18] B. A. Brown and W. D. M. Rae, Nucl. Data Sheets **120**, 115 (2014).
[19] M. Honma, T. Otsuka, B. A. Brown, and T. Mizusaki, Phys. Rev. C **69**, 034335 (2004).

[20] T. Rauscher and F. K. Thielemann, At. Data Nucl. Data Tables **75**, 1 (2000).
[21] J. S. Randhawa, R. Kanungo, J. Refsgaard, P. Mohr, T. Ahn, M. Alcorta, C. Andreoiu, S. S. Bhattacharjee, B. Davids, G. Christian, A. A. Chen, R. Coleman, P. E. Garrett, G. F. Grinyer, E. Gyabeng Fuakye, G. Hackman, J. Hollett, R. Jain, K. Kapoor, R. Krücken, A. Laffoley, A. Lennarz, J. Liang, Z. Meisel, B. Nikhil, A. Psaltis, A. Radich, M. Rocchini, N. Saei, M. Saxena, M. Singh, C. Svensson, P. Subramaniam, A. Talebitaher, S. Upadhyayula, C. Waterfield, J. Williams, and M. Williams, Phys. Rev. C **104**, L042801 (2022).
[22] C. Iliadis, *Nuclear Physics of Stars* (Wiley-VCH, Verlag, Wenheim, Germany, 2015).
[23] A. Sauerwein, M. Elvers, J. Endres, J. Hasper, A. Hennig, L. Netterdon, A. Zilges, Prog. Part. Nucl. Phys. **66**, 363 (2011).
[24] T Rauscher, N Dauphas, I Dillmann, C Fröhlich, Zs Fülöp, and Gy Gyürky, Rep. Prog. Phys. **76**, 066201 (2013).
[25] M. Wang, W. J. Huang, F. G. Kondev, G. Audi, S. Naimi, Chin. Phys. C **45**, 030003 (2021).
[26] S. E. A. Orrigo, B. Rubio1, W. Gelletly, P. Aguilera, A. Algora, A. I. Morales, J. Agramunt, D. S. Ahn, P. Ascher, B. Blank, C. Borcea, A. Boso, R. B. Cakirli, J. Chiba, G. de Angelis, G. de France, F. Diel, P. Doornenbal, Y. Fujita, N. Fukuda, E. Ganioğlu, M. Gerbaux, J. Giovinazzo, S. Go, T. Goigoux, S. Grévy, V. Guadilla, N. Inabe, G. G. Kiss, T. Kubo, S. Kubono, T. Kurtukian-Nieto, D. Lubos, C. Magron, F. Molina, A. Montaner-Pizá, D. Napoli, D. Nishimura, S. Nishimura, H. Oikawa, V. H. Phong, H. Sakurai, Y. Shimizu, C. Sidong, P.-A. Söderström, T. Sumikama, H. Suzuki, H. Takeda, Y. Takei, M. Tanaka, J. Wu, and S. Yagi, Phys. Rev. C **103**, 014324 (2021).
[27] S. F. Paul, J. Bergmann, J. D. Cardona, K. A. Dietrich, E. Dunling, Z. Hockenbery, C. Hornung, C. Izzo, A. Jacobs, A. Javaji, B. Kootte, Y. Lan, E. Leistenschneider, E. M. Lykiardopoulou, I. Mukul, T. Murböck, W. S. Porter, R. Silwal, M. B. Smith, J. Ringuette, T. Brunner, T. Dickel, I. Dillmann, G. Gwinner, M. MacCormick, M. P. Reiter, H. Schatz, N. A. Smirnova, J. Dilling, and A. A. Kwiatkowski, Phys. Rev. C **104**, 065803 (2021).
[28] E. Browne and J. K. Tuli, Nucl. Data Sheets **114**, 1849 (2013).
[29] C. Mazzocchi, Z. Janas, J. Döring, M. Axiotis, L. Batist, R. Borcea, D. Cano-Ott, E. Caurier, G. de Angelis, E. Farnea, A. Faßbender, A. Gadea, H. Grawe, A. Jungclaus, M. Kapica, R. Kirchner, J. Kurcewicz, S.M. Lenzi, T. Martínez, I. Mukha, E. Nácher, D. R. Napoli, E. Roeckl, B. Rubio, R. Schwengner, J. L. Tain, and C. A. Ur, Eur. Phys. J. A **12**, 269 (2001).
[30] M. J. López Jiménez, B. Blank, M. Chartier, S. Czajkowski, P. Dessagne, G. de France, J. Giovinazzo, D. Karamanis, M. Lewitowicz, V. Maslov, C. Miehé, P. H. Regan, M. Stanoiu, and M. Wiescher, Phys. Rev. C **66**, 025803 (2002).
[31] L. Kucuk, S. E. A. Orrigo, A. Montaner-Pizá, B. Rubio, Y. Fujita, W. Gelletly, B. Blank, Y. Oktem, T. Adachi, A. Algora, P. Ascher, R. B. Cakirli, G. de France, H. Fujita, E. Ganioğlu, J. Giovinazzo, S. Grévy, F. M. Marqués, F. Molina, F. de Oliveira Santos, L. Perrot, R. Raabe, P. C. Srivastava, G. Susoy, A. Tamii, J. C Thomas, Eur. Phys. J. A **53**, 134 (2017).
[32] W. Hauser and H. Feshbach, Phys. Rev. **87**, 366 (1952).
[33] T. Rauscher, N. Nishimura, R. Hirschi, G. Cescutti, A. St. J. Murphy, and A. Heger, Mon. Notices Royal Astron. Soc. **463**, 4153 (2016).
[34] W. Rapp, J. Görres, M. Wiescher, H. Schatz, and F. Käppeler, Astrophys. J. **653**, 474 (2006).
[35] G.Gürdal and F.G.Kondev, Nucl. Data Sheets **113**, 1315 (2012).
[36] Kazumasa Miyano, Hiromichi Nakahara, and Carmen Gil, J. Phys. Soc. Jap. **33**, 1505 (1972).
[37] M. Singh, J.W. Sunier, R.M. DeVries, and G.E. Thompson, Nucl. Phys. A **193**, 449 (1972).
[38] K. Oxorn, A.J. Houdayer, and S.K. Mark, Z. Phys. A **279**, 289 (1976).
[39] MIRCON MSD12 Circular Silicon Detector.
[40] MIRCON MSD26 Circular Silicon Detector.
[41] MIRION Low Energy Germanium Detector.
[42] MIRION Extended Range Coaxial Germanium Detector.
[43] MIRION Cryo-Pulse 5 PLUS Electrically Refrigerated Cryostat.
[44] MIRION Intelligent Preamplifier.
[45] XIA Pixie-16 Digitizer.
[46] XIA Pixie-16 Digitizer User Manual.
[47] B. E. Glassman, D. Pérez-Loureiro, C. Wrede, J. Allen, D. W. Bardayan, M. B. Bennett, K. A. Chipps, M. Febbraro, M. Friedman, C. Fry, M. R. Hall, O. Hall, S. N. Liddick, P. O'Malley, W. -J. Ong, S. D. Pain, S. B. Schwartz, P. Shidling, H. Sims, L. J. Sun, P. Thompson, and H. Zhang, Phys. Rev. C **99**, 065801 (2019).
[48] L. J. Sun, M. Friedman, T. Budner, D. Pérez-Loureiro, E. Pollacco, C. Wrede, B. A. Brown, M. Cortesi, C. Fry, B. E. Glassman, J. Heideman, M. Janasik, A. Kruskie, A. Magilligan, M. Roosa, J. Stomps, J. Surbrook, and P. Tiwari, Phys. Rev. C **103**, 014322 (2021).
[49] B. Singh and J. Chen, Nucl. Data Sheets **158**, 1 (2019).
[50] Ch. Miehé, Ph. Dessagne, Ch. Pujol, G. Walter, B. Jonson, and M. Lindroos, Eur. Phys. J. A **5**, 143 (1999).
[51] K. Starosta, C. Vaman, D. Miller, P. Voss, D. Bazin, T. Glasmacher, H. Crawford, P. Mantica, H. Tan, W. Hennig, M. Walby, A. Fallu-Labruyere, J. Harris, D. Breus, P. Grudberg, W.K. Warburton, Nucl. Instrum. Methods Phys. Res. A **610**, 700 (2009).
[52] C.J. Prokop, S.N. Liddick, B.L. Abromeit, A.T. Chemey, N.R. Larson, S. Suchyta, J.R. Tompkins, Nucl. Instrum. Methods Phys. Res. A **741**, 163 (2014).
[53] H.Y. Wu, Z.H. Li, H. Tan, H. Hua, J. Li, W. Hennig, W.K. Warburton, D.W. Luo, X. Wang, X.Q. Li, S.Q. Zhang, C. Xu, Z.Q. Chen, C.G. Wu, Y. Jin, J. Lin, D.X. Jiang, Y.L. Ye, Nucl. Instrum. Methods Phys. Res. A **975**, 164200 (2020).
[54] Matt Newville, easyXAFS, Matteo Levantino, Christian Schlepuetz, Damian Günzing, Max Rakitin, Sang-Woo Kim, and kalvdans, xraypy/XrayDB: (4.5.1). Zenodo (2023).
[55] D. Weisshaar, D. Bazin, P.C. Bender, C.M. Campbell, F. Recchia, V. Bader, T. Baugher, J. Belarge, M.P. Carpenter, H.L. Crawford, M. Cromaz, B. Elman, P. Fallon, A. Forney, A. Gade, J. Harker, N. Kobayashi, C. Langer, T. Lauritsen, I.Y. Lee, A. Lemasson, B. Longfellow, E. Lunderberg, A.O. Macchiavelli, K. Miki, S. Momiyama, S. Noji, D.C. Radford, M. Scott, J. Sethi, S.R. Stroberg, C. Sullivan, R. Titus, A. Wiens, S. Williams, K. Wimmer, S. Zhu, Nucl. Instrum. Methods Phys. Res. A **847**, 187 (2017).
[56] M. Basunia, Nucl. Data Sheets **107**, 2323 (2006).
[57] M. J. Martin, Nucl. Data Sheets **114**, 1497 (2013).
[58] Bé, M.-M. and Chisté, V. and Dulieu, C. and Mougeot, X. and Browne, E. and Chechev, V. and Kuzmenko, N. and Kondev, F. and Luca, A. and Galán, M. and Nichols, A.L. and Arinc, A. and Huang, X., Monographie BIPM-5 Table of Radionuclides Vol.5, Bureau International des Poids
[59] Chavdar Dutsov, Benoît Sabot, Philippe Cassette, Krasimir Mitev, Appl. Radiat. Isot. **176**, 109845 (2021).
[60] Marcell P. Takács, Karsten Kossert, Appl. Radiat. Isot. **176**, 109858 (2021).